Progress in Additive Manufacturing
https://doi.org/10.1007/s40964-024-00888-3

FULL RESEARCH ARTICLE

Numerical simulation of the shear rate in the fused filament fabrication process of poly-ether-ether-ketone (PEEK)

Shahriar Bakrani Balani[1,2] · Hossein Mokhtarian[1] · Tiina Salmi[2] · Eric Coatanéa[1]

Received: 5 September 2024 / Accepted: 17 November 2024

Abstract
Fused filament fabrication (FFF) is a material extrusion-based process and one of the most popular additive manufacturing processes, widely used for rapid prototyping and manufacturing of polymeric parts. Despite the simplicity of the process, the polymer undergoes complex rheological properties' transformation in this process. Understanding the rheological properties of the polymer during deposition is of paramount importance to model and improve the quality of the final product. In this study, for the first time, a two-phase flow numerical simulation approach with a Level Set equation has been used to model the shear rate in the FFF process after polymer exiting from the nozzle. The rheological properties of the raw PEEK as the feedstock were measured at low frequency by parallel-plate rheometer, and at high shear rate using an extensional die. Influence of travel speed, inlet velocity, nozzle diameter, and layer height on the shear rate of the deposited bead has been investigated. Obtained results revealed that the inlet velocity, nozzle diameter, and layer height highly influence the shear rate of the bead after exiting from the nozzle, while the influence of travel speed on the shear rate is negligible. Increasing the inlet velocity leads to an increase in velocity field and consequently maximum shear rate during deposition. Polymer melt tends to relax stress and become at steady state after existing from the nozzle rapidly, thus, it is required to reduce the inlet velocity using bigger nozzle diameter or smaller diameter raw filament or increase layer height to reduce the induced shear rate during deposition. Finally, multiple equations have been proposed to predict the maximum shear rate during the deposition based on the printing parameters.

Keywords Additive manufacturing · Material extrusion · Fused filament fabrication · Finite element simulation · Poly-ether-ether-ketone · PEEK · Rheological properties · Computation fluid dynamics

Abbreviations

3D	Three dimensional
AM	Additive manufacturing
CFD	Computational fluid dynamics
FFF	Fused filament fabrication
FIN	Flow identification number
LS	Level set
MEX	Material extrusion process
PEEK	Poly-ether-ether-ketone
PF	Phase-field
TFP	Two-phase flow
VOF	Volume-of-fluid

✉ Hossein Mokhtarian
hossein.mokhtarian@tuni.fi

[1] Engineering and Natural Science Faculty, Tampere University, Tampere, Finland

[2] Information Technology and Communication Science Faculty, Tampere University, Tampere, Finland

Latin symbols

a	Dimensionless viscosity transition index [1]
C_p	Specific heat capacity [J.(kg.K)$^{-1}$]
D_f	Filament diameter[mm]
d_n	Nozzle diameter [mm]
E	Length of extruded filament per command line [mm]
F	Other external forces [N]
F_{st}	Surface tension force [kg.(m.s^{-2})]
g	Gravity acceleration [m.s^{-2}]
H	Mean curvature
h	Coefficient of convection [W.(m^2.K)$^{-1}$]
H_i	Height of the layer [mm]
IV	Inlet velocity [mm.s^{-1}]
k	Coefficient of conduction [W.(m.K)$^{-1}$]
L	Length of the deposited bead [mm]
L_i	Initial length of the bead
n	Pseudoplasticity index [1]
n_i	Normal vector
P	Pressure [MPa]

Q_e	Crystallization exothermic heat [W]
r	Radial distance from the center axe in the nozzle [mm]
T	Temperature [°C]
T_b	Temperature of the deposited bead [°C]
T_c	Temperature of the printing chamber [°C]
T_p	Printing temperature [°C]
T_s	Temperature of substrate [°C]
TS	Travel speed [mm.s^{-1}]
$\vec{u}$	Velocity field [mm.s^{-1}]
V	Deposited melt volume [mm^3]
W_i	Initial wide of the bead [mm

Greek symbols

$\dot{\gamma}$	Shear rate of the bead [s^{-1}]
$\dot{\gamma}_n$	Shear rate in the nozzle [s^{-1}]
$\dot{\gamma}_s$	Shear rate applied from the substrate [s^{-1}]
$\overline{v}$	Mean inlet velocity in the nozzle [mm.s^{-1}]
η_0	Viscosity at terminal regime [Pa.s]
η_{inf}	Viscosity at infinity shear rate [Pa.s]
ε_{ls}	Interfacial thickness parameter [mm]
γ	Re-initialization parameter [m.s^{-1}]
δ	Dirac function
ε	Coefficient of surface emissivity [1]
η	Viscosity [Pa.s]
η^*	Complex viscosity [Pa.s]
ρ	Density [kg.m^{-3}]
σ	Surface tension [N.m^{-1}]
τ	Shear stress [MPa]
ω	Frequency [Hz]
λ	Relaxation time index [s]
φ	Volume fraction [1]

1 Introduction

Fused filament fabrication (FFF) is one of the most used additive manufacturing (AM) processes based on the material extrusion process (MEX) for polymeric materials. In this process, solid polymer in the form of filament or pellets is pushed into the extruder where they are melted using an electrical heater resistance surrounding the extruder. The melted polymer is then pushed out of the extruder through a printing nozzle on a predefined trajectory to manufacture the desired geometry by adhesion between the deposited beads and layers. The FFF process provides freedom of design while reducing the lead time by eliminating the need for use of material removing processes in the manufacturing chain. The simplicity and rapidity of the process make the FFF process convenient for manufacturing finished and semi-finished geometries. However, one of the main drawbacks of the manufactured part using the FFF process is the lack of mechanical strength [1]. Adhesion and bonding of the beads are the most crucial properties influencing the mechanical strength of the printed part as they directly influence the porosity of the printed geometry [2, 3]. Furthermore, rheological properties are the key factor influencing the printability of the polymer melt [4, 5]. Quality improvement of the manufactured parts requires delicate determination of the process properties such as rheological properties and temperature as they influence the stability, coalescence, and bonding of the adjacent beads [6, 7]. While conventional methods can be used to characterize the rheological properties of raw feedstocks in the form of filament and pellets [8], assessing the process rheological properties in the FFF process poses a significant challenge. Experimental study of the rheological properties is sometimes impossible or requires appropriate sensors and measuring methods which are usually expensive or require multidisciplinary expertise [9]. On the other hand, the analytical equations could only be used for the simple cases, and they are not applicable to the complex cases such as polymer melt flow after exiting from the nozzle [10]. Chen et al. constructed a low-cost device based on the pressure drop of the volumetric flow rate in the nozzle to determine the filament rheological properties during the FFF process [11]. Although these experimental studies are suitable for the determination of the rheological properties of the polymer melt in the nozzle and before exiting from the nozzle, they are not capable of determining the properties of the polymer when they are exiting from the nozzle. Thus, numerical simulation could be used as an alternative for modeling these properties for more complex cases by considering geometry and process parameters. Numerical simulation has been proven to be an adequate approach for the determination of the FFF process properties [12], especially for modeling the properties that are not possible or not cost-effective to determine by experimentally. This is specially the case for the determination of the rheological properties during material deposition in the FFF process, where the quality of the printed part is highly dependent on them [13, 14]. The computational fluid dynamics (CFD) modeling approach has been widely used for modeling the material extrusion processes [15]. Investigating the characteristics of the FFF process through numerical simulation involves addressing complex multi-phase fluid dynamics [16]. Various methodologies have been suggested to tackle the challenges of multi-phase numerical modeling in fluid dynamics. Notably, Level Set (LS) [17], Volume-of-fluid (VOF) [15, 18], and Phase-field (PF) [19] methodologies stand out as pivotal approaches for modeling two-phase flow (TPF) systems. Multiple authors have suggested integrating the two aforementioned modeling approaches as a strategy to address the limitations inherent in each individual method [20–23].

Mishra et al. [24] studied the viscosity based on the process parameters within the nozzle during the deposition.

In their studies, they have investigated the influence of the extrusion velocity, extrusion temperature, and material on the viscosity and density. Osswald et al. [25] introduced a coupled mass, momentum, and energy analytical model to predict the flow within the nozzle, as well as the melting rate in the FFF process. Gilmer et al. [26] introduced a method for efficiently evaluating polymer melt quality in the FFF process. By employing rheological analysis and tensile measurements, they anticipated the extrusion failures. The model outlines the velocity profile magnitude within FFF hot-end configurations, culminating in a singular dimensionless parameter known as the Flow Identification Number (FIN), which forecasts a material's tendency for backflow [26]. While extensive research has focused on the rheological properties of polymer melts within the nozzle during the FFF process, there remains a gap in understanding the shear rate of the polymer melt once it exits the nozzle. In the FFF process, the quality and mechanical integrity of printed parts are highly dependent on the material flow behavior during deposition. This flow behavior is influenced by the shear rate, which affects critical factors such as viscosity, layer adhesion, surface finish, and the occurrence of defects like warping and stringing [27, 28]. Determination of the shear rate during deposition is crucial to predict the quality of the deposited bead. Without a clear understanding of the shear rate effects, printing may encounter issues such as poor layer bonding, poor surface roughness, and dimensional inaccuracies. Furthermore, at a very high shear rate polymer melt undergoes the sharkskin effect which affects the quality of extruded bead [14]. Shear rate determination is also important for selecting appropriate materials, and developing new materials tailored for the FFF process. The shear rate and temperature of the deposited bead are the most important parameters influencing he viscosity and bonding of two adjacent deposited beads [6]. Theoretical models in literature like Rolie-Poly model or Doi-Edwards model are used to predict the behavior of polymer melts under deformation, considering factors like chain entanglements, reptation, and chain stretch. These models facilitate understanding the evolution of shear rate under processing conditions. Beside theoretical models, numerical simulations are alternative approaches to understanding and predicting the shear rate for more complex cases (for example, considering complex geometries and process parameters) [27].

This study aims to investigate the determination of shear rate during deposition process in the FFF, using the TPF numerical simulation approach. This work builds upon our previously published study [29]. In the earlier research, we developed a numerical simulation that could be used for modeling the shape of the deposited bead during the FFF process. The results for the shape of the deposited bead were compared to the experimental study to validate the numerical model. In the current study, we have used this numerical model to determine the shear rate in the FFF process based on the printing parameters.

To visualize the set of parameters/variables involved in this study and their relationships, a colored directed graph is developed using the dimensional analysis conceptual modeling (DACM) Framework [30, 31] as shown in Fig. 1. The developed causal graph serves as visual knowledge graph in this article. The independent variables (green) denote input process parameters or design variables, such as layer height (H_i), intended initial width of the bead (W_i), intended length of the bead (L_i), printing temperature (T_p), substrate temperature (T_S), temperature of the printing chamber (T_c), nozzle travel speed (TS), raw filament diameter (D_f), and filament inlet velocity (IV). Exogenous variables (grey) encompass factors external to the study's scope, while material properties remain fixed assumptions in the modeling. Dependent variables (blue) are influenced by both exogenous and independent variables, exemplified by inlet velocity (IV) in the graph. According to the graph, IV is influenced by the initial length of the bead (L_i), travel speed (TS), nozzle diameter (d_n), and the length of extruded filament per command line (E). Parameter E in broad term refers to the length of the filament feed to the extruder to ensure uniform material deposition based on the printing parameter settings while printing. Slicer software replaces the curvilinear movement and even long-distance linear movements with smaller linear movements define by G01 in G-code convention. Hence, the trajectory breaks in small linear steps. The length of the required filament extrusion is calculated by the slicer software based on the length of these steps. The slicer software automatically integrates this value for each line of the

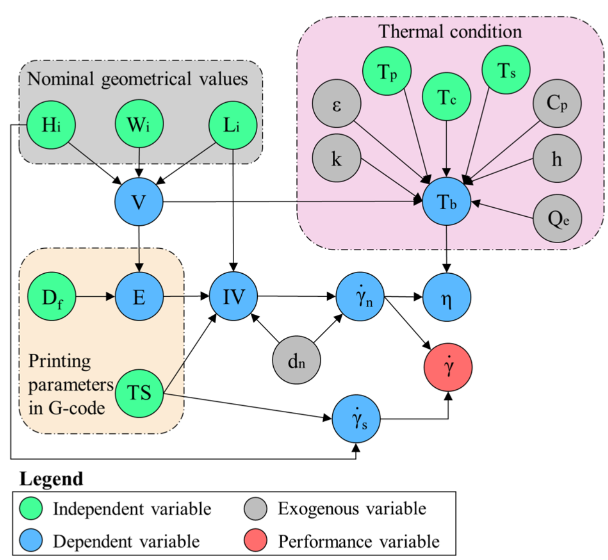

Fig. 1 Representation of colored direct graph of the parameters influencing shear rate of the FFF process

printing command. For instance, the command line G01 X20 Y35 E5 indicates that the printer moves linearly to destination coordinates (20, 35) while extruder feeds 5 mm of the filament. As depicted in Fig. 1, the shear rate in the FFF process comprises shear rates in the nozzle ($\dot{\gamma}_n$) and from the substrate ($\dot{\gamma}_s$). The performance variable constitutes the primary objective of the design and modeling, which in this context is the shear rate ($\dot{\gamma}$) during deposition in the FFF process.

In this article, we have selected poly-ether-ether-ketone (PEEK) as a high-performance thermoplastic. PEEK has high mechanical properties, chemical resistance [32], and operational temperature which make it suitable for high-end applications such as medical [33, 34], aerospace [35], electrical, and chemical [36]. The remainder of the manuscript is organized as the following: Sect. 2 describes the overall methodology and material used in this research. More specifically, Sect. 2 describes the material characterization and analytical background of the study of material deposition. Section 3 is articulated around the numerical simulation. The results and discussion section focuses on design of experience for conducting numerical simulations and study the influence of printing parameters such as H_i, nozzle diameter (d_n), IV, and TS on the shear during deposition. Determination of the shear rate of the deposited bead after exiting from the nozzle using numerical simulation is the key novelty of this research.

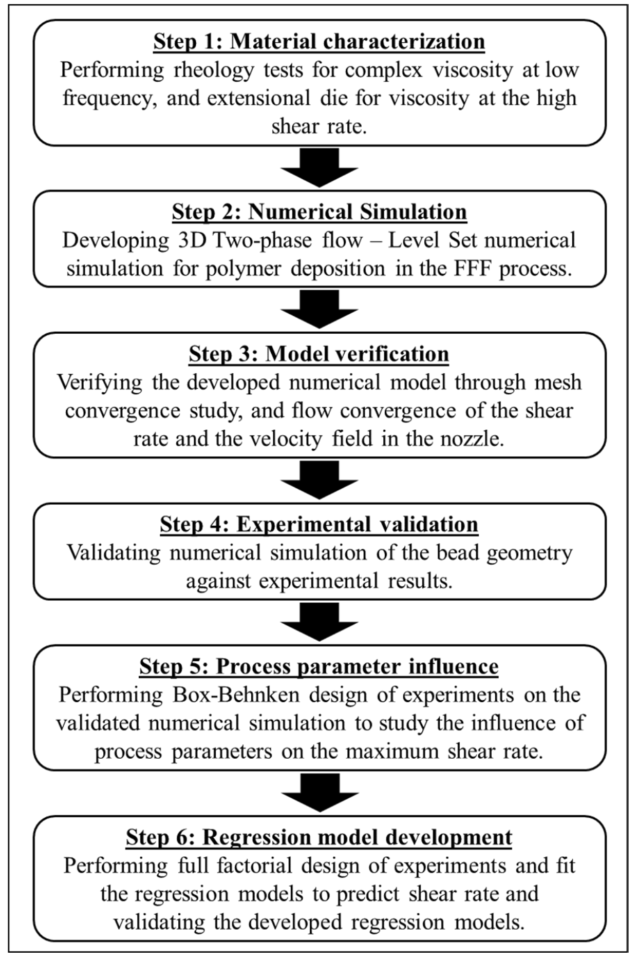

Fig. 2 Research methodology workflow

2 Materials and methods

The workflow of the study is represented in Fig. 2. In the first step, rheological properties of PEEK have been determined using rheometer at the low shear rate and an extensional die mounted on an extruder for the high shear rate. The Carreau–Yasuda viscosity equation has been fitted on the experimental data determined for viscosity. The results of this material characterization were fed to the numerical simulation in Step 2. Subsequently, a 3D numerical simulation using TPF simulation with LS equation is created to model the FFF process and deposition. Step 3 is dedicated to model verification where the validity of the developed numerical model is verified with mesh convergence study and convergence of shear rate and velocity field in the nozzle. In step 4, the numerical simulation of deposited bead geometry is experimentally validated. To investigate the influence of printing parameters on the maximum shear rate value in step 5, a Box–Behnken (BBD) design of experience has been performed on the validated numerical simulation. Step 6 of the current research focuses on the development and validation of the regression models on the developed simulations. These regression models could be used to predict the shear rate as a form of mathematical equation and replacing the numerical simulations.

2.1 Material characterization

PEEK 450G manufactured by Victrex has been selected as a feedstock in this study. The key process quality factors in the FFF process highly depend on the material properties such as thermal transitions, crystallization, and rheological properties. To eliminate moisture in raw pellets, the PEEK pellets were dried for 24 h at 140 °C in the oven and stored in the desiccator before further processing and testing. Due to the importance of the rheological properties, we have conducted two series of experimental studies to determine the viscosity of PEEK covering a wide range of shear rates (0.05 s^{-1}–10 000 s^{-1}):

i) Parallel-plate configuration of rheometer to determine the complex viscosity at low frequency (Shear rate) from 0.05 Hz to 100 Hz.

ii) Extrusion machine equipped with an extensional die for determination of the viscosity and shear rate above 100 s^{-1} until 10 000 s^{-1}. The schematic presentation of the die used for this study is illustrated in Fig. 4.

2.1.1 Determination of complex viscosity at the low shear rate with the rheometer

Rheometer is used to determine the complex viscosity according to the frequency. Based on the Cox-Merz rule the steady-state shear viscosity at a specific shear rate equals the complex viscosity at the corresponding frequency within the linear domain ($|\eta^*(\omega)| = \eta(\dot{\gamma} = \omega)$) [37]. The parallel-plate configuration consists of a fixed bottom plate and an upper rotational plate which applies a specific torque to the testing sample [38]. A 25 mm diameter disk with 2 mm thickness made of PEEK is used as the testing sample for the test. The PEEK plate is manufactured using a hot compression press. In a hot compression press, the temperature and pressure applied to the specimens are controlled. To decrease the surface roughness and protect the samples from any contamination, steel foil sheets were placed between the plates and the frame. The PEEK pellets are placed in a $150 \times 75 \times 2$ mm^3 mold (with a metallic frame) and heated at 10 ˚C.min^{-1} until melting temperature (360 ˚C). The mold is maintained at 360 ˚C under 70 kN pressure for 10 min. Then the plate is cooled down to 140 ˚C with a cooling rate of 10˚C.min^{-1}. The above-mentioned procedure leads to the manufacturing of thermally stable plates.

The manufactured sample by the hot press is then used for the frequency sweep test by a parallel-plate configuration for a frequency range of 0.05 to 100 rad.s^{-1} at a 1% strain level. As represented in Fig. 3, different temperature points above the melting temperature are selected for the experiments: 350 ˚C, 366 ˚C, 383 ˚C, and 400 ˚C. As anticipated for the molten polymers, PEEK exhibits a shear-thinning behavior with a Newtonian plateau at the lower frequencies. At 1 rad.s^{-1}, the complex viscosity is 5841 Pa.s at 350 ˚C, 5144 Pa.s at 366 ˚C, 4413 Pa.s at 383 ˚C, and finally, 3292 Pa.s at 400 ˚C. The complex viscosity determined experimentally indicates that the increase in temperature and frequency results in a decrease in viscosity. For high temperature and low frequency, viscosity of PEEK increases drastically. For the highest temperatures, the molecular chains of PEEK undergo recombination of molecular bond degradation and chain branching [39]. This structural modification has consequences on the properties of the polymer when the polymer is exposed to high temperature for a long time (hereby for frequencies below 0.1 Hz). To extrapolate the complex viscosity at the lower shear rate, the time–temperature superposition could be used.

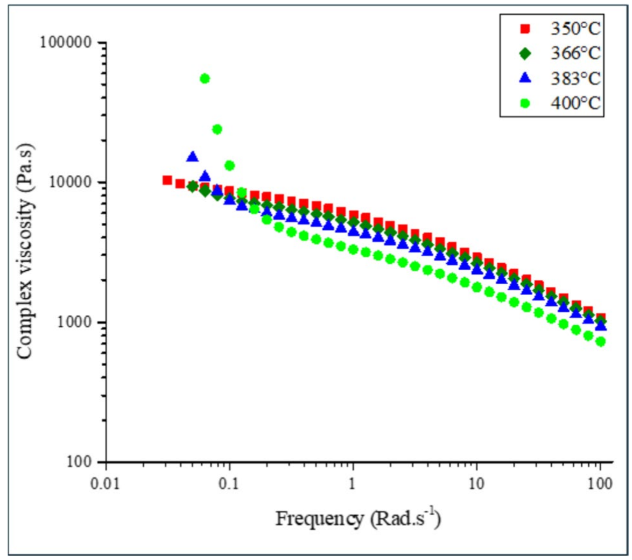

Fig. 3 Complex viscosity (η*) of PEEK determined by the parallel-plate configuration for the viscosity at low frequency (shear rate) (0.05–100 Hz)

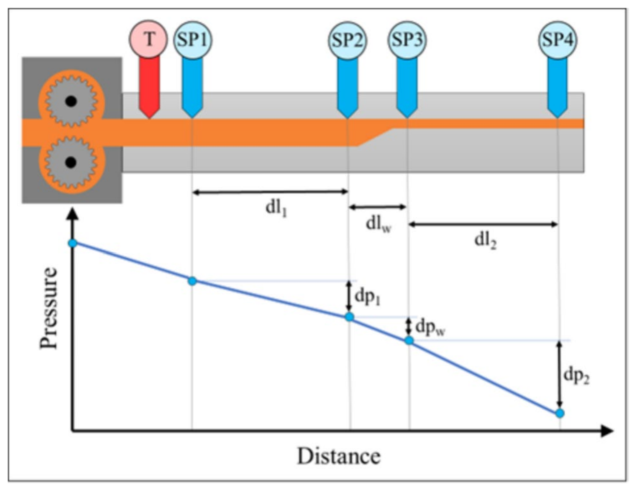

Fig. 4 Schematic presentation of the die used to determine the viscosity at high shear rate and extensional viscosity (adopted from [40])

2.1.2 Determination of viscosity at high shear rate using extensional die

Rheometer is not suitable for determination of the viscosity at higher frequencies. Additionally, determining the extensional viscosity of the polymers is not possible with this configuration of the rheometer. Therefore, an extruder equipped with an extensional die manufactured by ThermoFisher® is used to determine the viscosity at the shear rate the higher than 100 s^{-1}. Unlike the rheometer where the fluid is under shear, in the extensional die the fluid (or polymer) is under extensional stress. Using this die, viscosity of the polymers at high shear rate up to 10 000 s^{-1} could be determined. A schematic presentation of the die used for this study is illustrated in Fig. 4. The die has three different regions to determine the viscosity at different regimes. The first region, which is between SP1 and SP2 pressure sensors is used to determine the viscosity at low shear rate. The second region is between SP2 and SP3 pressure sensors, which is suitable to determine the extensional (elongation) viscosity in this section of the die polymer is under extensional stress. The third part of the die is used to determine the viscosity at high shear rate between SP3 and SP4 pressure sensors.

Figure 5 illustrates the results for the viscosity determined by the two experimental methods at 383 °C. Complex viscosity is represented by a red square, and the shear viscosity determined by the extensional die is depicted by black triangle (for the low shear rate) and green diamonds (for the high shear rate). At very high shear rate, viscosity is drastically reduced to 40 Pa.s. Furthermore, the extensional viscosity determined by the die is represented in black circles. The results obtained with the extensional die below 50 s^{-1} show a good correlation with those obtained with the parallel-plate rheometer. In the following studies on shear rate, the shear viscosity is used for fitting the Carreau–Yasuda equation and not the extensional viscosity.

2.2 Analytical bases

2.2.1 Fitting Carreau–Yasuda equation on the experimental data

The Carreau–Yasuda model is commonly used to describe the non-Newtonian behavior of polymers. A nonlinear

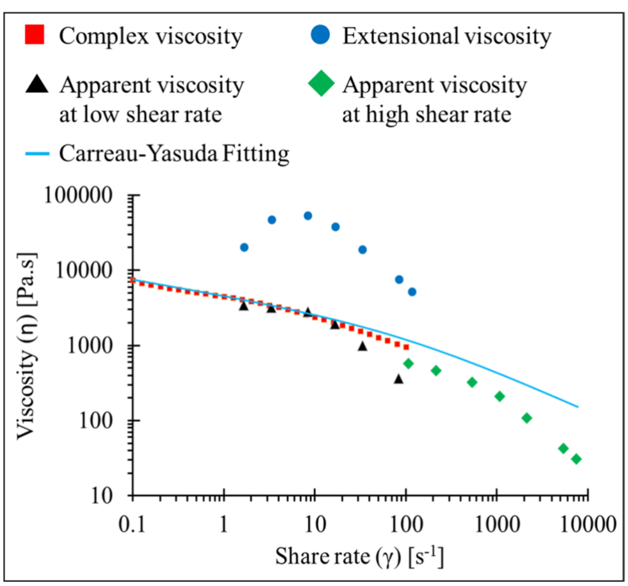

Fig. 5 Viscosity of PEEK at 383 °C

regression using the least-squares fitting method was used to fit the Carreau–Yasuda model on the experimental rheological data, where the viscosity was measured as a function of shear rate (Eq. 1). Carreau–Yasuda model defines viscosity as a function of shear rate while taking into account the Newtonian plateau at low shear rate [38].

$$\eta = \eta_{inf} + \left(\eta_0 - \eta_{inf}\right)\left[1 + (\lambda\dot{\gamma})^a\right]^{\frac{n-1}{a}} \tag{1}$$

where n is the pseudoplasticity index, η_0 is the viscosity of the fluid at zero shear rate, η_{inf} is the viscosity of the fluid at an infinite shear rate, λ is the relaxation time index, a is a dimensionless parameter describing the transition between the first Newtonian plateau and power law zone and, $\dot{\gamma}$ is the shear rate. Thermoplastics are the shear-thinning fluids with pseudoplasticity index (n) below one (1), which means by increasing the shear rate, viscosity decreases. The Carreau–Yasuda model of the viscosity is superposed on the experimental data determined by rheometer (Sect. 2.1.1) and extensional die (Sect. 2.1.2) for complex viscosity and shear viscosity, respectively. The terms of the Carreau–Yasuda model have been extracted from the fitting of the viscosity curves on the points are provided in Table 1. In the following studies, the viscosity of PEEK is inserted as the Carreau–Yasuda model, which enables the determination of the viscosity according to the shear rate.

2.2.2 Shear rate determination in the FFF process

As represented in Fig. 6, two sources of shear rate are applied on the polymer melt in the FFF process: shear rate due to the shear stress in the nozzle (similar to the fluid flow between two fixed walls) which is called Poiseuille flow and shear rate applied from the moving nozzle on the deposited polymer bead still in the melted state (similar to the fluid flow between a fixed wall and a moving wall) which is known as Couette flow [14, 41]. In the case of the Poiseuille flow, the shear rate is dependent on the inlet velocity (IV) (Eq. 2) and nozzle diameter (d_n) and could be determined analytically using Eq. 4 for the shear-thinning polymers (Fig. 7).

Table 1 Values of the Carreau–Yasuda parameters for T = 383 °C

Parameter (Symbol)	Value
Viscosity at infinity shear rate (η_0)	7071 ± 153 Pa.s
Viscosity at terminal regime (η_{inf})	0 Pa.s
Relaxation time index (λ)	1.45 ± 0.6 s
Dimensionless viscosity transition index (a)	0.78 ± 0.12
Pseudoplasticity index (n)	0.59 ± 0.06

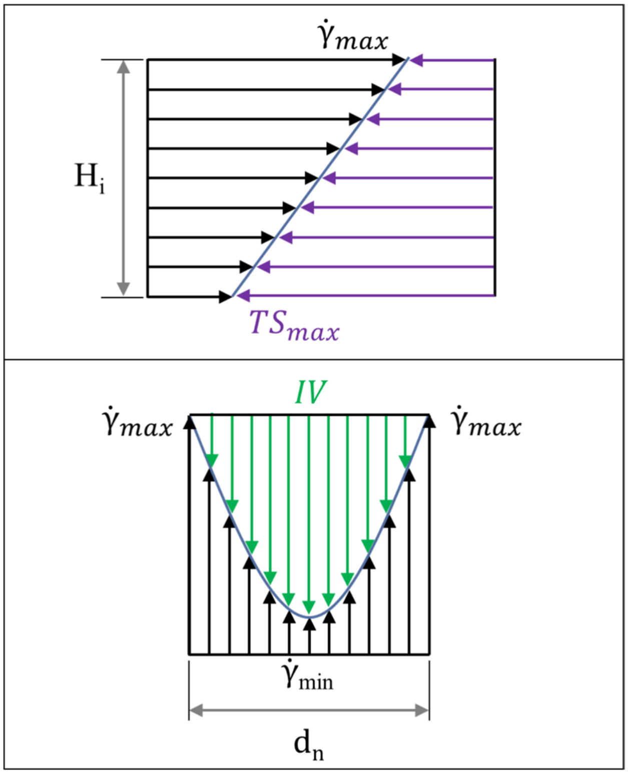

Fig. 6 Schematic presentation of two sources of shear rate in the FFF process; up) shear rate applied to the deposited polymer melt due to the TS; down) shear rate applied to the polymer melt in the nozzle

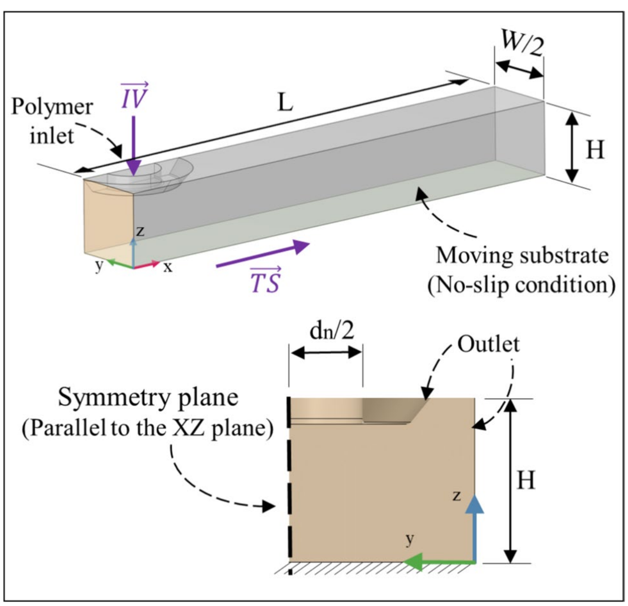

Fig. 7 Boundary conditions of 3D model developed for the material deposition

The average inlet velocity ($\overline{IV}$) of the of the filament in the nozzle could be written as a function of printing parameters (TS, L), d_n, D_f, and (Eq. 2) [29]:

$$\overline{IV} = \frac{E * TS * {D_f}^2}{L * d_n^2} \tag{2}$$

The velocity field and shear rate in the nozzle could be determined according to the rheological properties of the fluid by Eq. 3 and Eq. 4, where n is the pseudoplasticity index from the Carreau–Yasuda equation, and d_n is the nozzle diameter [14]:

$$\vec{u}(r) = \frac{3n+1}{n+1}\overline{IV}\left[1 - \left(\frac{r}{0.5 * d_n}\right)^{\frac{(1+n)}{n}}\right] \tag{3}$$

$$\dot{\gamma} = \frac{3n+1}{n * 0.5 * d_n} * \overline{IV} * \left[\left(\frac{r}{0.5 * d_n}\right)^{\frac{1+n}{n}-1}\right] \tag{4}$$

where r is the position from the center. In the case of Couette flow, shear rate and viscosity between a moving surface and a fixed surface are $\frac{TS}{H_i}$ and $\frac{\tau}{\dot{\gamma}}$, respectively.

3 Numerical simulation modeling

3.1 Numerical modeling and boundary conditions

3D numerical simulation of material deposition has been previously created using the two-phase flow (TPF) with Level set (LS) approach in COMSOL Multiphysics 6.1 [42]. TPF-LS modeling is suitable for modeling a system of two immiscible fluids (in the case of material deposition air and polymer melt), where two fluids are separated through an interface [42]. In this modeling approach, the velocity field (u, w, v) of each fluid is determined with respect to the other fluid and applied forces to the system with the Navier–Stokes and continuity equations (Eq. 5 and Eq. 6) [42]. For material deposition of the polymers, because the Reynolds number is very small (below 0.001) the inertia term of the Navier–stokes is neglected. Thus, there is a laminar flow in the nozzle and when exiting from the nozzle. That means, there is no turbulence when polymer exists from the nozzle. The deposited bead is in isothermal condition, and there is no heat transfer between the deposited bead and ambient when the polymer exists from the nozzle. The main reason for this assumption is that the shear rate is measured immediately in 0.2 s after the deposition. Consequently, the polymer melt does not have time for heat transfer with the ambient. Furthermore, there is no external tension or extensional flow (stretching or extension along one or several directions) on the polymer melt when exiting the nozzle.

Consequently, the fluid flow is determined using the Stokes Equation (Eq. 6):

$$\nabla.\vec{u} = 0 \tag{5}$$

$$\nabla.\left[-pI + \eta(\nabla\vec{u} + \left(\nabla\vec{u}\right)^{T})\right] + \rho g + \sigma H\delta n_i + F = 0 \tag{6}$$

where ρ represents density, u stands for fluid velocity, p represents the pressure exerted on the fluid, η denotes the viscosity of the fluid, σ represents surface tension coefficient, H stands for mean curvature, δ is the Dirac function, n_i denotes the normal vector and g represents the gravitational field. $\sigma H\delta n_i$ is associated with surface tension, while F includes all remaining external forces.

The velocity field determined by Stokes and continuity equations for two fluids does not track the interface between two fluids. Consequently, an additional transport equation must be added to them for tracing the boundary between two fluids. LS equation (Eq. 7) is a well-known transport equation for tracking the interface of two immiscible fluids. With the LS equation, the volume fraction (φ) as an auxiliary variable is determined for tracking the interface of the two fluids. In the TPF-LS modeling system volume fraction varies between 0 and 1. The value 0 is devoted to fluid 1 (in our case air) and the value 1 is fluid 2 (in our case polymer melt) and 0.5 represents the interface of two fluids [42]. In other words, φ = 0.5 represents the boundary of the air and polymer. Boundary is evolving according to the velocity field of two fluids (air and polymer). When value of φ is more than 0.5, the associate region is filled with polymer and when it is less than 0.5, it represents the air.

$$\frac{\partial\varphi}{\partial t} + \nabla.(\vec{u}\varphi) = \gamma\nabla.\left(\varepsilon_{ls}\nabla\varphi - \varphi(1-\varphi)\frac{\nabla\varphi}{|\nabla\varphi|}\right) \tag{7}$$

γ is the re-initialization parameter, and ε_{ls} is the parameter controlling the interfacial thickness. Reducing ε_{ls} results in a more accurate interface between two fluids; however, reducing it makes numerical model more prone to numerical instability. In our studies, maximum velocity of the fluid in the TPF system is selected as the initial value for γ. Viscosity and density in the TPF system are determined as a function of volume fraction (Eq. 8 and Eq. 9).

$$\rho = \varphi\rho_{polymer} + (1-\varphi)\rho_{air} \tag{8}$$

$$\eta = \varphi\eta_{polymer} + (1-\varphi)\eta_{air} \tag{9}$$

where $\rho_{polymer}$ and ρ_{air} are the densities of polymer and air, respectively, $\eta_{polymer}$ and η_{air} are the viscosities of the polymer and air, respectively.

To reduce the computation time, half of the geometry is modeled, and the symmetrical boundary condition are applied to other half of the geometry. The details of the boundary conditions are represented in our previous publication [29]. No-slip boundary condition is defined for the extruder surface which is in contact with polymer melt (nozzle). A moving wall with no-slip condition with 30° contact angle is selected for the contact between the substrate and polymer melt. The 30° contact angle is selected based on our experimental studies. The surface tension of PEEK at molten state is estimated to be 0.018 N m^{-1}, using the Parachor equation [43]. The density value of 1300 kg m^{-3} was derived from datasheet provided by Victrex [44]. The reinitialization parameter (γ) sets to 15 mm s^{-1}, and parameter controlling interface thickness (ε_{ls}) is kept at default value.

Two segregated studies are selected: one for determination of parameter φ and the second one for determination of velocity field and pressure. The GMERS solver is used for both LS and fluid flow variables determination. The absolute tolerance for the time-dependent solver is 0.05. Free tetrahedral mesh type with the normal physics-controlled mesh size is applied to all the models. Based on the variable values, each model has between 1.7 million and 2 million degrees of freedom. To refine the mesh near the nozzle and substrate, an adaptive mesh is applied to the model. Near the substrate, the boundary layer mesh is applied to the model.

A presentation of the mesh is illustrated in Fig. 8. Selected time step is 0.025 s and total simulation time is 1 s.

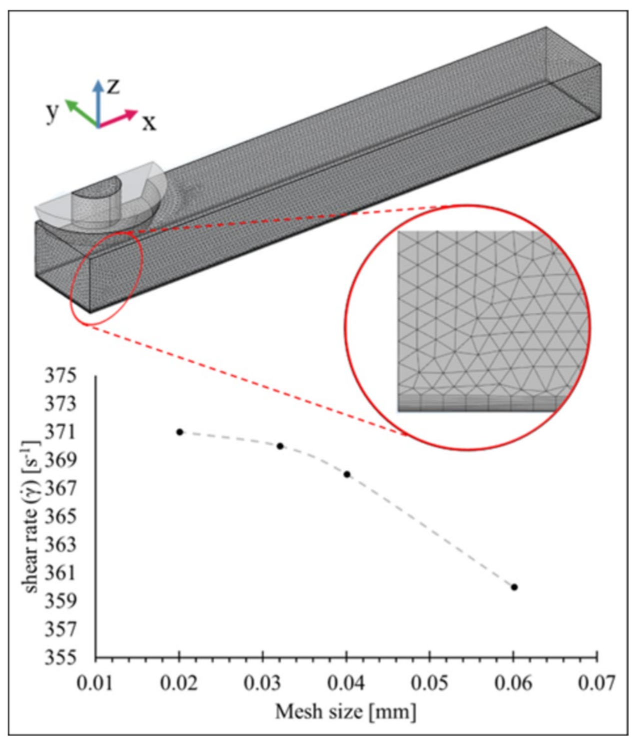

Fig. 8 Presentation of the meshed model for the numerical simulation and sensitivity of the shear rate to the mesh size

The mesh size in LS modeling needs to be adjusted according to the LS equation parameters (ε_{ls} and γ). Using a coarse mesh size results in numerical errors or wrong values for the shear rate. The calculation time for a case with 1.85 million degrees of freedom is approximately 7 h and 20 min. The sensitivity of the shear rate to mesh size is investigated for various mesh sizes. As can be seen in Fig. 8, for a specific case study at the lower mesh size the shear rate is converging toward 371 s^{-1}. Consequently, a maximum mesh size of 0.025 mm is assigned to the geometry.

Obtained results of polymer deposition according to time for $H_i = d_n = 0.4$ mm, IV = 0.25 mm.s^{-1}, and TS = 20 mm.s^{-1} is shown in Fig. 9. As represented in Fig. 9, polymer exits from the nozzle and is deposited on the mobile platform continuously until forming the bead geometry.

4 Results and discussion

4.1 Design of experiments (DOE)

In the first step and to determine the impact of input process parameters (stated in Fig. 1) on the shear rate during material deposition, a design of experiment (DOE) approach has been followed. BBD has been adopted to study the effect of H_i, d_n, IV, and TS, including 27 experiments (4 factors with 3 levels each) using developed numerical simulation. Table 2 represents the 27 experiments of BBD DOE with the maximum shear rate in the location P2, in which rows 6, 15, 2, and 26 are repetitions. Further analysis in this article is performed only on the point where maximum shear rate takes place (location point P2). However, Annex 1 tabulates the results in other location points P1–P5. Location P1 refers to the point close to the substrate, along the bead height (on the line perpendicular to the substrate). Location P2 is where the shear rate reaches the maximum value on the same line as P1 (along the bead height or on the perpendicular line to substrate). Location P3 is close to the nozzle, and P4 represents the location point where the shear rate is at the maximum value, along the bead length (on the line parallel to the substrate). P5 is the relaxation point where polymer melt is no longer under influence of TS and extrusion. Figure 10 schematically represents the location of P1–P5.

BBD is a response surface method used to generate a higher order response surface. Generating the response surface with BBD requires fewer experiments compared to the full factorial and central composite design. For instance, BBD requires 27 experiments, while full factorial DOE requires 81 experiments to cover 4 factors with 3 levels each. In addition, BBD avoids the extreme corner points compared to the central composite design. Another aim of DOE was to detect and exclude the parameter(s) which their influence on the shear rate is negligible. The analysis of the main effect plots reveals that TS does not influence the shear rate after deposition (see Sect. 4.4). Hence, a second DOE is conducted as a full factorial to present a complete set of results. The second DOE is a full factorial DOE, in which TS is considered constant to the (25 mm s^{-1}) is shown in Table 4 in Sect. 4.5.

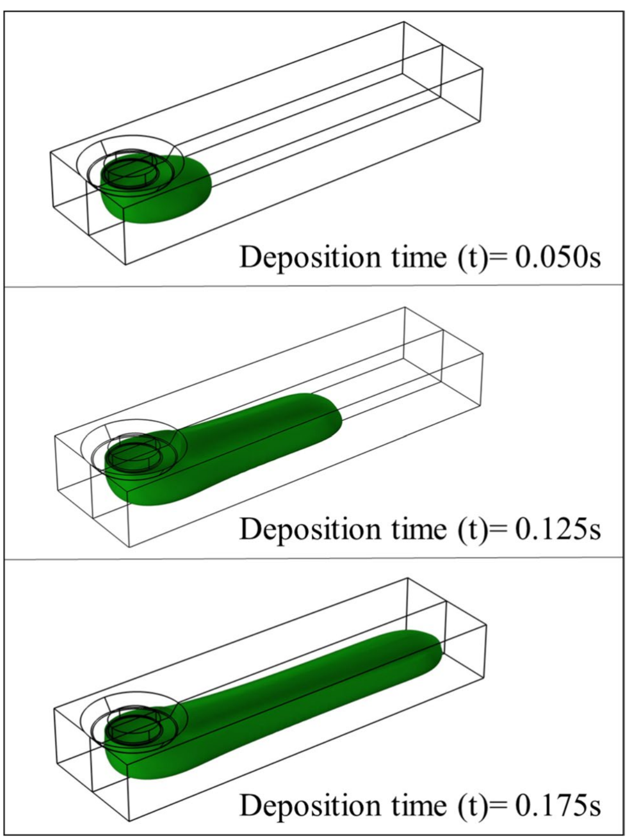

Fig. 9: 3D presentation of the material deposition on the substrate (dn0.4 mm, IV0.25 mm s^{-1}, TS20 mm s^{-1})

4.2 Investigation of the fluid flow convergence in the nozzle

In the extruders, polymer melt flows through the extruder with a diameter equivalent to the filament diameter (here 1.5 mm) to the nozzle with a diameter varying from 0.25 mm to 0.5 mm. The diameter change in the extruder causes a perturbation in the fluid as polymer melt flows through the nozzle. Consequently, it is important to select the nozzle length with respect to the convergence of the fluid flow and reducing the perturbation of the melt flow. Otherwise, the perturbation caused by diameter change influences the shear rate and leads to wrong values and instability of the polymer bead. This is also a step toward the validation of the numerical model developed for the shear rate examination. The convergence study of the fluid flow could be done by examining

Table 2 A BBD DOE for studying the parameters influencing the shear rate

Run	H_i [mm]	d_n [mm]	IV [mm.s^{-1}]	TS [mm.s^{-1}]	IV/TS [--]	Max. shear rate at P2 location [s^{-1}]
1	0.25	0.4	50	25	2	721 ± 8
2	0.25	0.2	30	25	1.2	506 ± 2
3	0.3	0.3	40	30	1.33	490 ± 10
4	0.25	0.3	50	30	1.67	712 ± 10
5	0.25	0.4	40	30	1.33	570 ± 10
6	0.25	0.3	40	25	1.6	568 ± 10
7	0.3	0.2	40	25	1.6	702 ± 5
8	0.25	0.2	40	20	2	696 ± 2
9	0.2	0.3	30	25	1.2	538 ± 2
10	0.3	0.3	30	25	1.2	370 ± 10
11	0.2	0.3	50	25	2	907 ± 3
12	0.2	0.2	40	25	1.6	738 ± 10
13	0.25	0.3	50	20	2.5	729 ± 5
14	0.25	0.2	40	30	1.33	683 ± 2
15	0.25	0.3	40	25	1.6	568 ± 10
16	0.25	0.3	30	30	1	410 ± 10
17	0.2	0.4	40	25	1.6	711 ± 3
18	0.2	0.3	40	20	2	710 ± 10
19	0.25	0.4	40	20	2	574 ± 6
20	0.25	0.3	30	20	1.5	424 ± 5
21	0.3	0.4	40	25	1.6	474 ± 1
22	0.3	0.3	40	20	2	506 ± 5
23	0.3	0.3	50	25	2	630 ± 10
24	0.2	0.3	40	30	1.33	712 ± 5
25	0.25	0.4	30	25	1.2	426 ± 8
26	0.25	0.3	40	25	1.6	568 ± 10
27	0.25	0.2	50	25	2	872 ± 10

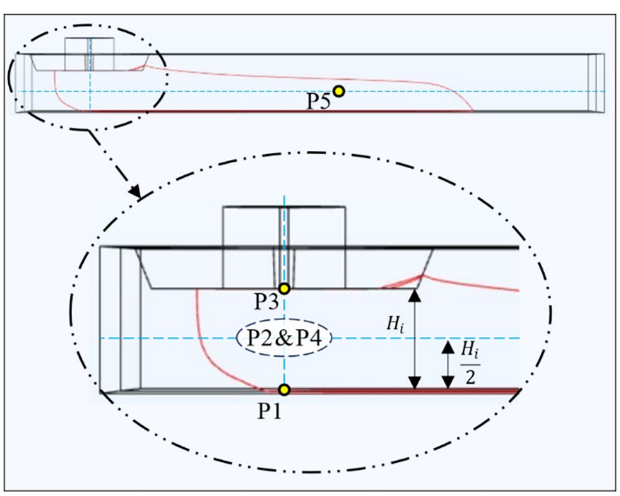

Fig. 10 Schematic representation of locations P1 to P5 in this study

shear rate and velocity field in the nozzle. As polymer flows through the nozzle, shear rate and velocity field must converge toward a fixed value in a parabolic shape and overlap each other. As depicted in Fig. 11, to study the flow convergence in the nozzle, four zones (lines L1–L4 in Fig. 11) are selected along the nozzle length between the nozzle inlet and outlet. The nozzle inlet is the zone where polymer melt enters the nozzle from the extruder with a larger diameter and the outlet is the orifice of the nozzle where polymer exits from the extruder for the deposition. L1 is selected close to the inlet and L4 is selected close to the outlet (see Fig. 11). Obtained results for the velocity field and shear rate along the diameter for the selected lines are illustrated in Fig. 11. In L1, close to the inlet, the shape of the velocity field curve is mostly linear at around 0.03 m.s^{-1}, and the shear rate at the center is non-zero around 200 s^{-1} while toward the outlet of the nozzle, it becomes parabolic shape, and maximum value is close to 0.05 m s^{-1} and shear rate is close to zero. Comparison between the obtained results for L1 to L4 revealed that the velocity field and shear rate are

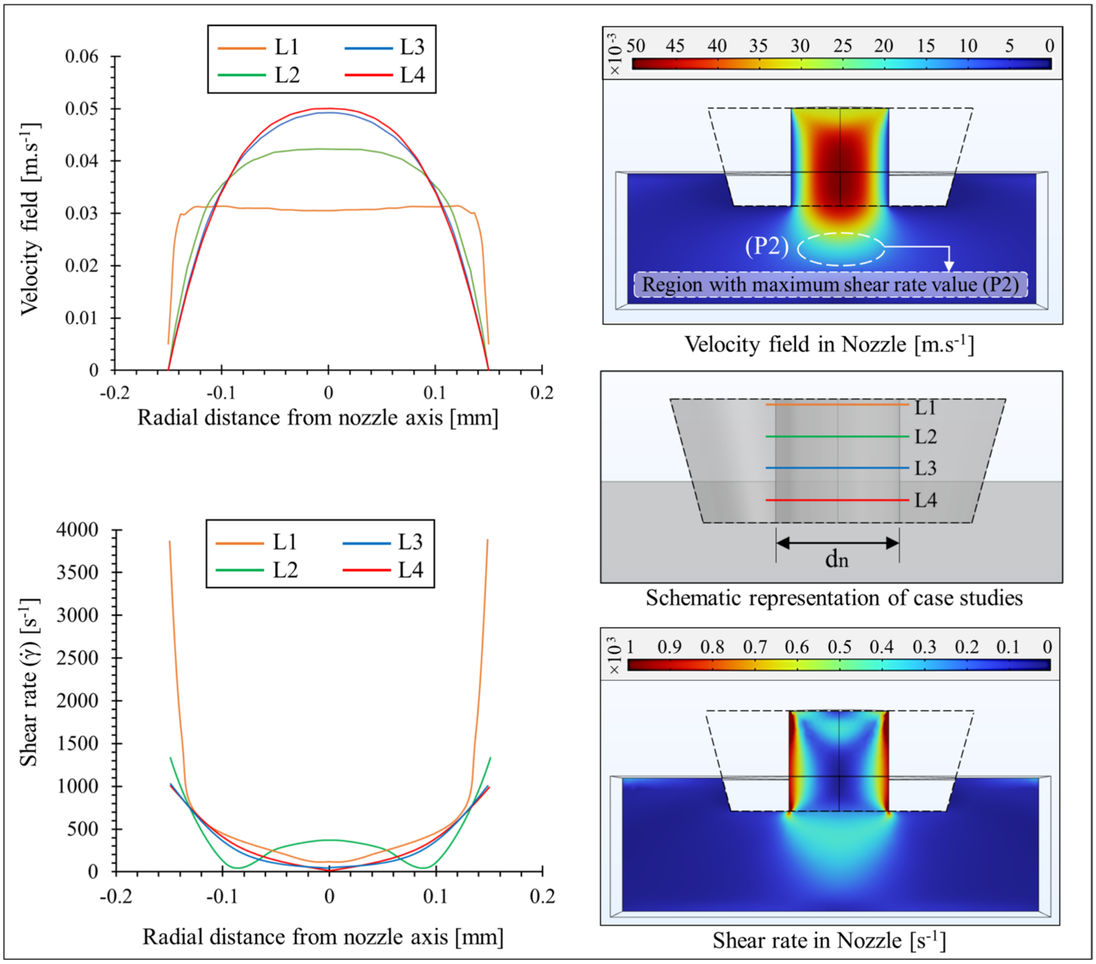

Fig. 11 Convergence of the velocity field and shear rate of fluid in the nozzle–Region where the maximum shear rate takes place (P2) is schematically shown in the top-right side

converging toward the same value as they get closer to the outlet of the nozzle. The convergence of the results toward the same values shows the importance of nozzle length to reduce the perturbation of the polymer melt flow when there is a change in the diameter of the internal extruder. The results also validate the selected geometry for the length of the nozzle in this study. The shear rate and velocity field in the nozzle determined by numerical simulation are validated with the analytical equations (Eq. 3 and Eq. 4) [14]. The numerical simulation revealed that the nozzle's length must be at least 0.2 mm to reach the convergence of the fluid flow in the nozzle.

4.3 Experimental validation of the numerical model

In Sects. 3.1 and 4.2, developed numerical model has been numerically validated through mesh convergence study, the convergence of the velocity field, and the shear rate profile in the nozzle. This section aims for experimental validation.

The developed numerical model for determination of the shear rate during deposition can also predict the bead geometry. Hence, the results obtained by numerical model for the shape of the deposited bead (width of the bead) are compared and validated by experimental study. Geometry of the deposited bead is a function of the velocity field of the material extruder and shear rate is derivative of the velocity field, thus, validating the shape of the deposited bead indirectly validates the shear rate during deposition.

In the current study, surface tension, density, and viscosity are the material properties input for the numerical simulation. Surface tension of PLA and PEEK at the melted state are 0.028 N m^{-1} and 0.018 N m^{-1}, respectively. These values are close to each other, thus, their differences in values does not exhibit an influence on the shear rate. On the other hand, densities of both polymers are also very close: density of PLA is 1250 kg mm^{-3} while PEEK is 1300 kg mm^{-3}. Therefore, density also does not exhibit any difference in the shear rate either. Furthermore, as shown in the literature, viscosity does not affect om the shape of the deposited geometry [29, 45].

We have studied shear rate in the nozzle for both PLA and PEEK. For a specific case study, maximum shear rate in the nozzle for PLA is 900 s^{-1} and for PEEK is 950 s^{-1}. The values of maximum shear rate in the nozzle for PLA and PEEK are close together. Their differences are even less for the shear rate after exiting from the nozzle. The closeness of the values for surface tension, the density for PLA and PEEK as well as the negligible influence of viscosity on the shear rate value in the nozzle, allow us to compare the results for PLA and PEEK.

Shear rate of PEEK and PLA for the same printing parameters are also determined for the flow when exiting from the nozzle. The results of the numerical model for the shear rate reveal that these polymers' shear rate values are close together. As an example, for TS15 and IV20, shear rate of PEEK and PLA are 235 s^{-1} and 238 s^{-1}, respectively. This is in line with the analytical equations (Eq. 3 and Eq. 4) as the shear rate and velocity field only depend on the pseudo-plasticity index (n). Consequently, as expected, fluid flow and shape of the bead are independent from the viscosity of the polymer [29]. Figure 12 represents the cross section of the deposited bead, after being cut along its cross-section. The image of cross section is recorded using a using a Leica (Wetzlar, Germany) DM2500M binocular with a 2 × magnifier lens. As represented in Fig. 12, the width of the bead determined by numerical simulation for PLA and PEEK results in the same value. Consequently, the numerical model is validated for PLA as a polymer which is widely used for the FFF process. The width of the bead determined experimentally is in good accordance with the numerical simulation for PLA.

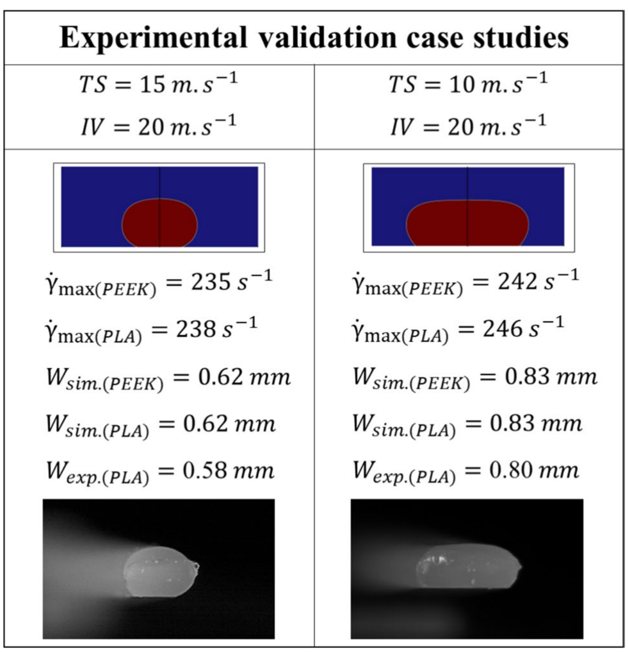

Fig. 12 Experimental validation of the numerical model in two case studies

4.4 Investigation of the parameters influencing shear rate during material deposition

The shear rate of the polymer melt as it exits the nozzle is a combination of two major sources. Polymer melt between the nozzle and deposition platform like one fixed plate and one moving plate. The second origin of the shear rate in the FFF process is the material flow in the nozzle and the extent of polymer melt flow after exiting from the nozzle. The shear rate applied to the polymer in both cases has been determined and compared to the shear rate in the FFF process when both cases are applied at the same time. Figure 13 and Fig. 14 represent the shear rate in XZ and YZ plans for the following three cases:

Case I (shear rate while extruding material): In this case, TS is 0 and IV is kept constant to a non-zero value (Hi0.3TS00IV20). The maximum shear rate is approximately in the middle of the H_i between the nozzle and substrate on the axis line passing through the center of the nozzle.

Case II (shear rate while substrate moves): This case investigates the shear rate between two parallel planes. The shear rate is applied between the nozzle and moving substrate with zero IV with fixed TS (Hi0.3TS20IV00). The maximum shear rate is approximately in the middle of the H_i between the nozzle and substrate.

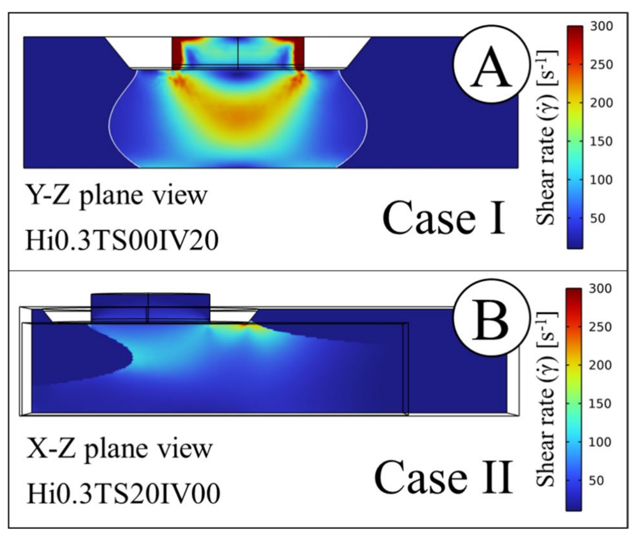

Fig. 13 Two components of the shear rate applied in the FFF process; **A** Shear rate while extruding material (Case I); **B** Shear rate while substrate moves (Case II)

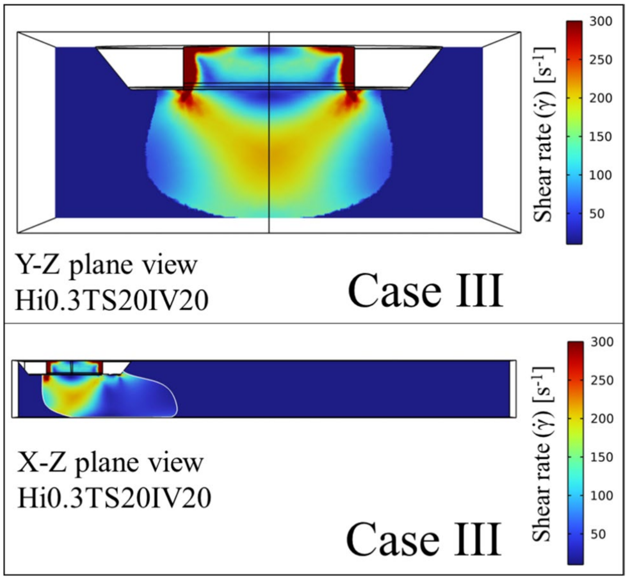

Fig. 14 Shear rate applied to the polymer melt in the FFF process (Case III)

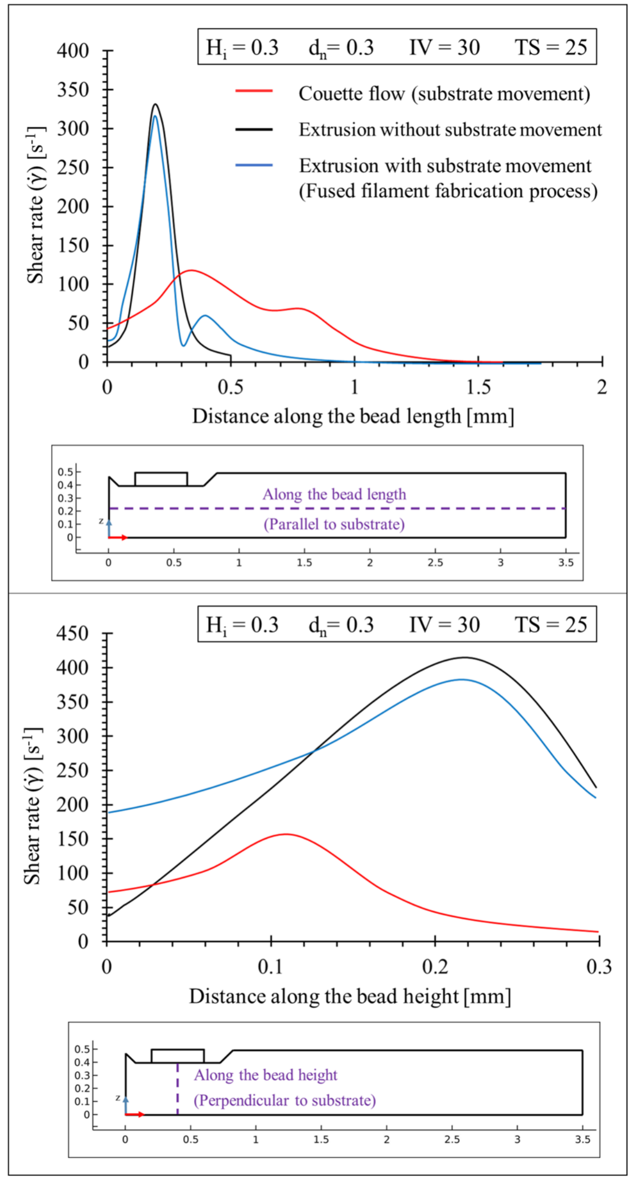

Fig. 15 Shear rate applied to the polymer melt after exiting from the nozzle for three cases; Top: Along the bead length (on the line parallel to the deposition substrate); Bottom: Along the bead height (on the line perpendicular to the deposition substrate)

Case III (shear rate in the FFF process): This case is the combination of two previous cases (Case I and II) and mimics the material deposition in the FFF process with non-zero IV and TS (Hi0.3TS20IV20).

To be more concise, the parameter settings of the case study are reported in the form of a chain of the variable acronym (symbol) followed by the associated set values. For instance, Hi0.3TS20IV20 indicates that $H_i = 0.3$ mm, TS = 20 mm s^{-1}, and IV = 25 mm s^{-1}.

The color plots of the shear rate applied to the polymer melt during deposition for all the 3 cases are illustrated in Fig. 13 and Fig. 14. Figure 13 illustrates the first two cases, and Fig. 14 shows the FFF process which is the combination of two cases. Contrary to the shear rate in the nozzle where in the center of the nozzle shear rate is about 0, simulations highlight that the maximum shear rate during deposition occurs on the line passing through the center of the nozzle. However, the location of the maximum shear rate depends on the value of TS and H_i. It is worth mentioning that even though the shear rate in the nozzle reaches above 5 000 s^{-1}, to better present/visualize the shear rate after exiting from the nozzle, we have limited the shear rate upper bound to 300s^{-1}, as shown in the legend of the figures. All the shear rate values above 300 s^{-1} are presented in dark red. The observations confirm that shear rate highly depends on the location of the polymer melt on the substrate and time. Once the deposition takes place, the shear rate gradually reduces to zero. However, the maximum shear rate during the deposition for the fixed parameters is constant and independent of time.

The shear rate curves on the parallel and perpendicular lines to the substrate are represented in Fig. 15. Maximum shear rate in the FFF process for this set of input is approximately 410 s^{-1} while the shear rate in the extrusion process (case I) and Couette flow (case II) is approximately 380 s^{-1} and 155 s^{-1}, respectively. Maximum shear rate peak in the FFF process and extrusion process are located in the same location, however, the peak of the shear rate in the Couette flow is shifted in the direction of the moving platform. In the FFF process and Couette flow an additional peak in the shear rate is observed which is the influence of the nozzle structure (metallic part) on the polymer melt. The shear rate in the FFF process (Case III) is not merely the sum of the shear rate while extruding material (Case I) and while the substrate moves (Case II). This is due to the difference in the direction of the velocity field applied in the FFF to the polymer melt. While the peak of the shear rate curve in the FFF process and extrusion is relatively in the same spot, peak due to the TS is about 0.2 mm lower in the Z-axis.

Shear rate in the FFF process depends on the printing parameters (IV, TS, H_i), and d_n, and rheological properties of the used polymer (pseudoplasticity index (n) in the Carreau–Yasuda equation). Figure 16 shows the influence of printing parameters on the shear rate at the perpendicular and parallel lines to the substrate. Shear rate curves allow us to compare the effect of printing parameters on the shear rate at the given locations. Comparing shear rate curves for TS20 and TS25 shows that the maximum shear rate on the deposited bead is independent of the TS. The maximum value of the shear rate is observed for the higher value of IV and lower H_i. Increasing IV leads to an increase in shear rate while decreasing H_i and d_n results in shear rate increase. This is in line with the conclusion derived from the shear rate equation presented in Eq. 4. Increasing IV leads to an increase of the mean IV in the nozzle ($\overline{IV}$) in the shear rate equation. On the other hand, increasing d_n leads to an increase of d_n in the dominator of the equation (Eq. 4) and consequently decrease in the shear rate.

BBD DOE has been performed on the developed numerical simulations to further analyze the effects of H_i, d_n, IV, and TS on the maximum shear rate at location point P2. Table 2 and Annex 1 represent the DOE table. Figure 17 presents the main effect plot illustrating the influence of four key printing parameters (H_i, d_n, IV, and TS) on the maximum shear rate, particularly at location point P2. Notably, the analysis reveals that the influence of TS on the shear rate is minimal, indicating that alterations in TS do not significantly affect the shear rate at the designated location point (P2). Furthermore, the main effect plot indicates that increasing H_i decreases the shear rate while increasing IV leads to an increase in the shear rate. Contrary to TS and IV, the influence of d_n on the shear rate is not linear. As represented in Fig. 17, increasing d_n mostly leads to a decrease in shear rate, however, slight increase is observed for the 0.4mm. The main reason for the nonlinear behavior of d_n could be related to the measuring point of the shear rate. Additionally, in an extrusion nozzle, the material being extruded experiences a high shear rate near the internal extrusion surface and a zero-shear rate at the center of the nozzle (according to Eq. 4). This effect occurs due to the no-slip conditions, velocity gradient, and viscous flow. Once the polymer melt exists the extrusion, the velocity gradient diminishes. The flow is less restricted, and the velocity becomes more uniform across the cross-section, and leading to a reduction of

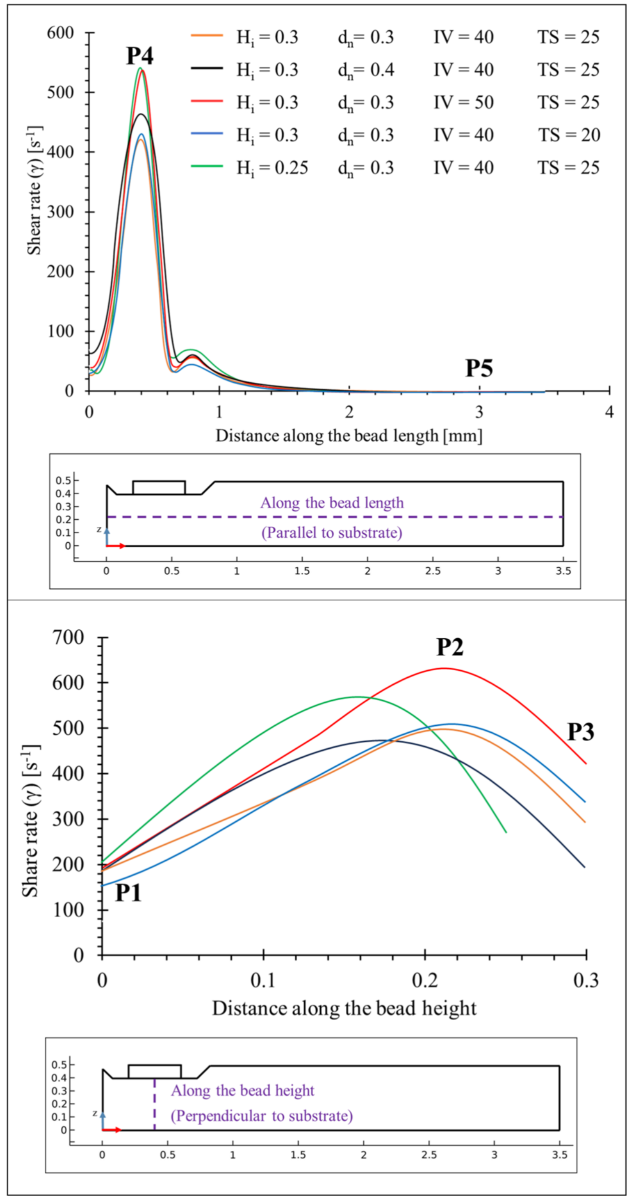

Fig. 16 Influence of the printing parameters on the shear rate of the deposited bead; Top: Along the bead length (Parallel to the deposition substrate) at the center of the nozzle; Bottom: Along the bead height (Perpendicular to the deposition substrate) at Z0.2 mm

the shear rate. Therefore, when polymer exists the nozzle, it is no longer under the effect of nozzle confinement. Consequently, it could be concluded that at a nozzle length of more than 0.3 mm, the shear rate is independent of the nozzle size.

Figure 18 illustrates the interaction plots between the involved parameters (H_i, d_n, IV, and TS) for the maximum shear rate at location P2. On the interaction plots for IV, the parallel curves indicate that there is no interaction between IV and H_i and d_n. However, the cross lines on the interaction plots reveal that interaction effects exist (For instance, see green and red dash lines in nozzle interaction plot for the

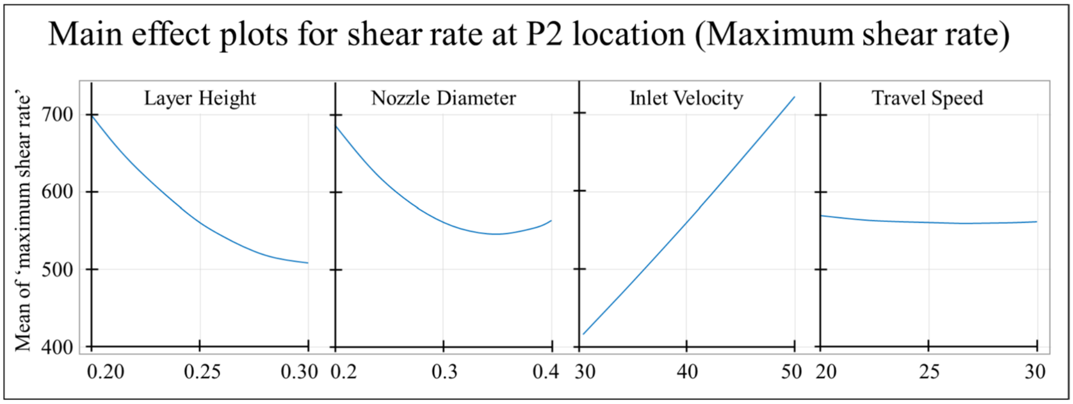

Fig. 17 Main effect plot for influencing parameters on shear rate at P2 location

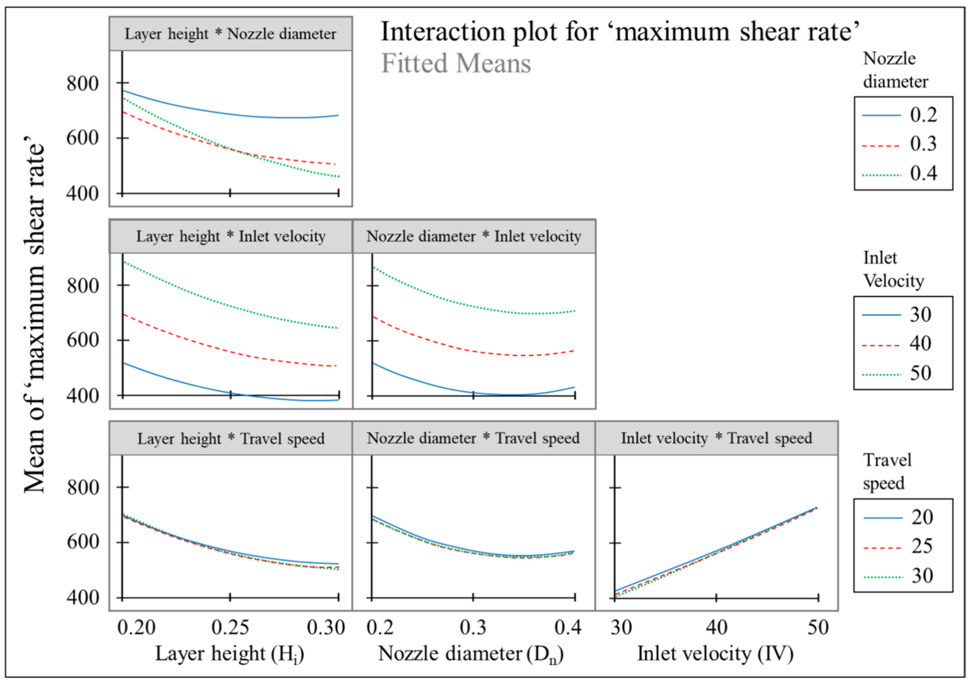

Fig. 18 Interaction plot for maximum shear rate (Location point P2)

d_n). Figure 19 illustrates the counter plots of the shear rate at the location point of P2 for three different d_n (0.2, 0.3, and 0.4), while the TS value is held to 25 mm s^{-1}. As can be seen from the plots, the minimum shear rate at P2 is in the range of 500–600 s^{-1} for $d_n = 0.2$ mm, while the minimum shear rate at P2 is even below 400 s^{-1} for the bigger nozzles.

Table 4 represents the full factorial DOE for 3 factors (H_i, d_n, and IV) with 3 levels each. Note that 13 experiments among the total 27 experiments in full factorial design are common with the BBD experiments (rows with even numbers in Table 2). Therefore, only 14 new simulations are performed to complete the full factorial design of experiments. Note that the data of DOE are collected by changing process parameters in one validated numerical model, hence duplicating of data from DOE 1 to DOE 2 does not perturbate the results, as opposed to experimentally collected data. Similarly to the previous DOE table, Annex 2 also represents the results in other location points (P1–P5).

4.5 Regression fitting on the shear rate data

The ultimate objective of this article is to present one or multiple mathematical models for predicting the shear rate without performing complex numerical simulations. Two regression models are fitted to predict the maximum shear rate (at the location point P2) as the response variable. The multiple regression technique is implemented on the full factorial DOE, shown in Table 4. In the first model, the nozzle diameter is considered as a categorical parameter, and continuous variables are IV and H_i. Equation 10 shows

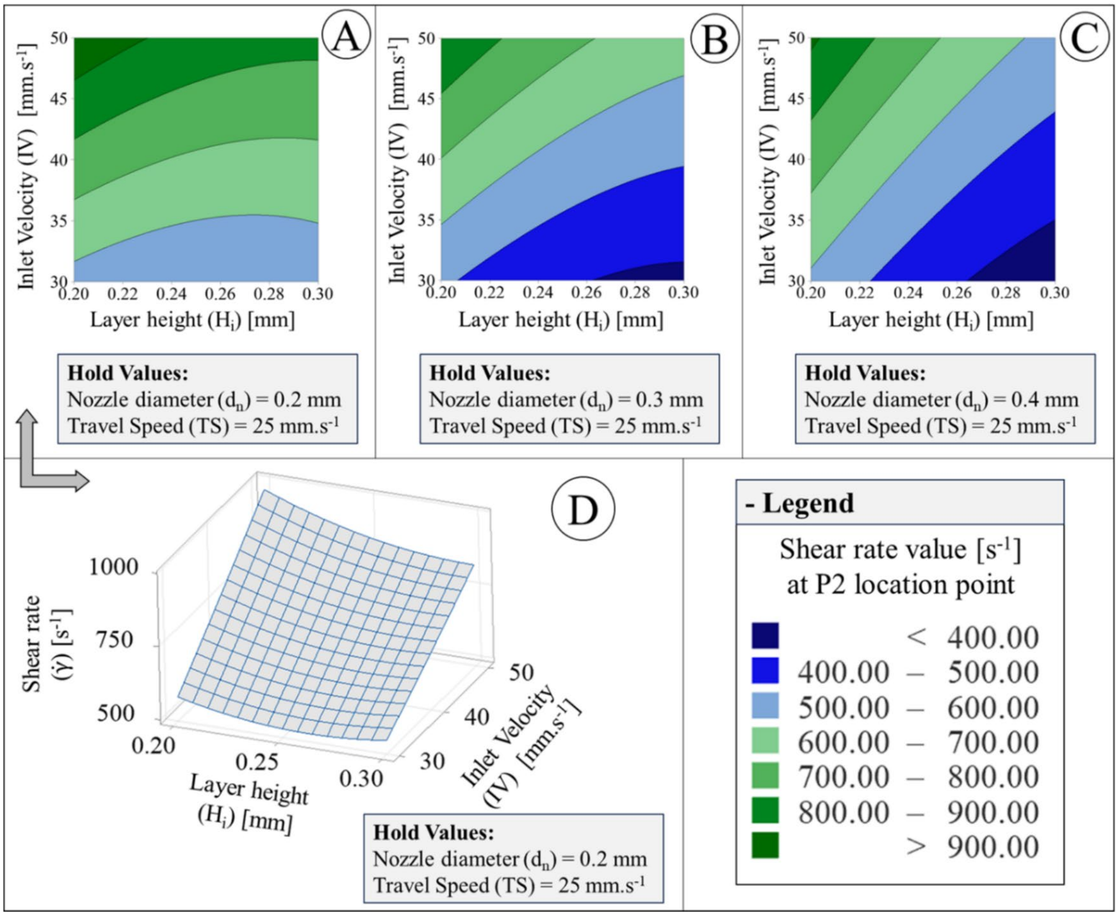

Fig. 19 Counter plots of the shear rate at location point of P2 vs. IV and H_i for d_n of 0.2, 0.3, and 0.4 mm (respectively **A**, **B**, and **C**); Surface plot of shear rate at location point of P2 vs. IV and H_i for $d_n = 0.2$ mm and TS = 24 mm s^{-1} (**D**)

Table 3 The coefficients of regression 'model 1' determined for different d_n

	$d_n = 0.2$ mm	$d_n = 0.3$ mm	$d_n = 0.4$ mm
A	402	881	924
B	28.96	25.58	25.08
C	4978	6808	6941
D	12,356	12,356	12,356
E	39.83	39.83	39.83

the general form of the regression model, where A, B, C, and D are the constant coefficients that are chosen based on the nozzle diameter from Table 3. Practically, it means that there is a unique equation for each nozzle diameter. Regression model 1 shows an R^2 value of 99.80%, indicating high accuracy.

$$\dot{\gamma} = A + B * IV - C * H_i + D * H_i^2 - E * IV * H_i \quad (10)$$

In the second regression model, d_n is also considered as a continuous variable, together with IV and H_i. Hence, Eq. 11 represents the data in full factorial DOE (Table 4). The R^2 value of the second regression model is 98.74%. As expected, the second regression model represents a lower R-squared value compared to the first regression model created separately for each d_n.

$$\dot{\gamma} = 388 + 32.36 * IV - 3297 * H_i - 526 * d_n + 12356 * H_i^2 + 5222 * d_n^2 - 39.8 * IV * H_i - 19.42 * IV * d_n - 9817 * H_i * d_n \quad (11)$$

The predictions of both regression models, as well as their relative error compared to the simulation results are calculated and tabulated in Table 4. The results show the average relative error of 1.09% and 2.44% (in full factorial DOE) for first and second regression models, respectively. Note that these regression models are developed on the full factorial dataset where the maximum shear rate value (at location P2) was the response variable.

Table 4 Full factorial DOE for studying the influence of printing parameters on the shear rate (TS = 25 mm.s^{-1}), regression models and their relative error percentage

Run	H_i	d_n	IV	$\dot{\gamma}_{max}$ at P2	$\dot{\gamma}_{Model1}$	%RE Model1	$\dot{\gamma}_{Model2}$	%RE Model2
1	0.2	0.2	30	540	530.46	1.77%	549.32	1.73%
2	0.2	0.2	40	738	740.4	0.33%	754.48	2.23%
3	0.2	0.2	50	944	950.34	0.67%	959.64	1.66%
4	0.2	0.3	30	538	542.06	0.75%	503.22	6.46%
5	0.2	0.3	40	719	718.2	0.11%	688.96	4.18%
6	0.2	0.3	50	907	894.34	1.40%	874.70	3.56%
7	0.2	0.4	30	533	543.46	1.96%	561.56	5.36%
8	0.2	0.4	40	711	714.6	0.51%	727.88	2.37%
9	0.2	0.4	50	887	885.74	0.14%	894.20	0.81%
10	0.25	0.2	30	506	499.82	1.22%	504.61	0.27%
11	0.25	0.2	40	692	689.85	0.31%	689.87	0.31%
12	0.25	0.2	50	872	879.87	0.90%	875.13	0.36%
13	0.25	0.3	30	414	419.92	1.43%	409.43	1.11%
14	0.25	0.3	40	568	576.15	1.43%	575.27	1.28%
15	0.25	0.3	50	722	732.37	1.44%	741.11	2.65%
16	0.25	0.4	30	426	414.67	2.66%	418.68	1.72%
17	0.25	0.4	40	572	565.9	1.07%	565.10	1.21%
18	0.25	0.4	50	721	717.12	0.54%	711.52	1.31%
19	0.3	0.2	30	516	530.97	2.90%	521.68	1.10%
20	0.3	0.2	40	702	701.08	0.13%	687.04	2.13%
21	0.3	0.2	50	886	871.19	1.67%	852.40	3.79%
22	0.3	0.3	30	370	359.57	2.82%	377.41	2.00%
23	0.3	0.3	40	497	495.88	0.23%	523.35	5.30%
24	0.3	0.3	50	630	632.19	0.35%	669.29	6.24%
25	0.3	0.4	30	346	347.67	0.48%	337.58	2.43%
26	0.3	0.4	40	474	478.98	1.05%	464.10	2.09%
27	0.3	0.4	50	604	610.29	1.04%	590.62	2.22%
					Average	1.09%	Average	2.44%

5 Conclusion

In the FFF process, the disentanglement of the macromolecular chains at the weld interface between the beads is influenced by both shear rate within the nozzle and degree of disentanglement. To accurately characterize the strength of the weld between printed filaments, it is crucial to understand the polymer behavior during extrusion, considering factors such as material properties, printing parameters, and nozzle geometry. Once material is deposited, the printed melt rapidly cools down toward the glass transition. How deformation relaxes as a function of temperature indicates the diffusive behavior at the weld, which is essential for understanding the final welding characteristics, including weld thickness, structure, and entanglement. Determination of the shear rate allows us to determine the relaxation time and to understand the diffusive behavior of polymer. Therefore, in this paper, we have focused on developing numerical simulation to study the shear rate applied to the polymer melt after exiting from the nozzle for PEEK. The assumptions for numerical simulation are laminar fluid flow, isothermal condition, and there is no external force or extensional flow. The shear rate of the polymer melt after exiting the nozzle is especially important because it directly influences viscosity, which in turn governs the coalescence and bonding of the deposited beads. Prior to studying the shear rate in the FFF process, it is required to measure the viscosity of raw material and express it as the renown Carreau–Yasuda Equation. ConsEquently, the viscosity of PEEK has been studied at low frEquency (shear rate) using the parallel-plate configuration of the rheometer and at high shear rate using an extensional die mounted on an industrial extruder machine at 383 °C. Viscosity is provided as a function of shear rate by superposition of the Carreau–Yasuda Equation on the experimental points. Shear rate-dependent viscosity expressed in the form of the Carreau–Yasuda Equation has been used as an input for the numerical simulation for determination of the shear rate applied to the polymer melt after exiting from the nozzle. At a very high shear rate (10,000 s^{-1}) viscosity of PEEK is reduced to approximately

10 Pa.s. A drastic increase of complex viscosity is observed at a very low frEquency (less than 0.05 Hz) and high temperature. This is due to the recombination of the molecular chains. As a result, determination of the complex viscosity at high temperatures and low shear rate is impossible by the parallel-plate configuration of the rheometer. The numerical model has been validated for mesh convergence, fluid flow convergence in the nozzle, and experimental study for the width of the bead. The bead's width is indirectly influenced by shear rate, the derivate of the velocity field. The influence of printing parameters (H_i, TS, d_n, and IV) on the shear rate has been investigated by TPF numerical simulation. The shear rate in the FFF process is a combination of the shear rate applied to the polymer passing through the nozzle and Couette flow, which are applied to the polymer melt at the same time. The plot effect of the parameters revealed that TS does not influence the shear rate while increasing IV and decreasing H_i leads to an increase in the shear rate. The maximum shear rate during deposition could reach more than 800 s^{-1} based on the selected printing parameters. Shear rate of the deposited bead is highly dependent on the coordinate of the point and gradually reduces as polymer melt rests on the substrate. To increase the viscosity and improve the coalescence between the deposited bead it is required to reduce the H_i and increase the IV and d_n. Finally, to predict the maximum shear rate applied to the polymer melt without performing numerical simulation, four equations have been proposed in this paper. Developed numerical simulation and its associated regression models hold the potential to be used as supplementary knowledge in the development of physics-based or knowledge-based machine learning models. For instance, Nagarajan et al., have integrated a numerical simulation to predict viscosity within their knowledge-based artificial neural networks (KB-ANN) to reduce the number of experimental trials required for training and validation [46]. Similarly, the developed numerical simulation offers an additional level of knowledge to enhance the machine learning models. The simulation allows the determination of the shear rate during deposition, while it is not experimentally measurable during the material deposition. In the future works we will concentrate on integration of the shear rate during deposition into the entanglement models and determination of degree of entanglement between the layers.

Annex 1: Box-Behnken design of experiment—4 variables with 3 levels—27 experiments

Run order	H_i	d_n	IV	TS	IV/TS	Shear rate at P1 (near substrate)	Shear rate at P2 (max perpend.)	Shear rate at P3 (near nozzle)	Shear rate at P4 (max parallel)	Shear rate at P5 (at relaxing point
1	0.25	0.4	50	25	2	200 ± 10	721 ± 8	363 ± 5	721 ± 10	2.5 ± 0.1
2	0.25	0.2	30	25	1.2	235 ± 15	506 ± 2	357 ± 1	296 ± 6	0.3 ± 0.01
3	0.3	0.3	40	30	1.33	226 ± 10	490 ± 10	336 ± 1	413 ± 2	0.6 ± 0.02
4	0.25	0.3	50	30	1.67	247 ± 3	712 ± 10	429 ± 1	672 ± 5	0.8 ± 0.01
5	0.25	0.4	40	30	1.33	230 ± 5	570 ± 10	277 ± 1	570 ± 2	1 ± 0.05
6	0.25	0.3	40	25	1.6	204 ± 5	568 ± 10	271 ± 5	541 ± 10	0.16 ± 0.0.1
7	0.3	0.2	40	25	1.6	200 ± 10	702 ± 5	509 ± 5	289 ± 6	0.18 ± 0.01
8	0.25	0.2	40	20	2	181 ± 5	696 ± 2	443 ± 1	416 ± 5	0.3 ± 0.01
9	0.2	0.3	30	25	1.2	278 ± 5	538 ± 2	235 ± 2	537 ± 1	0.4 ± 0.05
10	0.3	0.3	30	25	1.2	182 ± 10	370 ± 10	250 ± 2	305 ± 1	0.55 ± 0.05
11	0.2	0.3	50	25	2	350 ± 5	907 ± 3	410 ± 1	900 ± 2	1.6 ± 0.1
12	0.2	0.2	40	25	1.6	306 ± 5	738 ± 10	435 ± 2	614 ± 2	0.5 ± 0.02
13	0.25	0.3	50	20	2.5	228 ± 5	729 ± 5	459 ± 1	694 ± 5	1.3 ± 0.1
14	0.25	0.2	40	30	1.33	285 ± 10	683 ± 2	486 ± 1	394 ± 3	0.4 ± 0.02
15	0.25	0.3	40	25	1.6	204 ± 5	568 ± 10	271 ± 5	536 ± 10	0.16 ± 0.0.1
16	0.25	0.3	30	30	1	240 ± 15	410 ± 10	250 ± 5	385 ± 7	0.5 ± 0.01
17	0.2	0.4	40	25	1.6	279 ± 5	711 ± 3	373 ± 2	710 ± 1	2 ± 02
18	0.2	0.3	40	20	2	227 ± 3	710 ± 10	333 ± 3	713 ± 5	2.4 ± 2
19	0.25	0.4	40	20	2	161 ± 5	574 ± 6	290 ± 1	580 ± 3	1.6 ± 0.1
20	0.25	0.3	30	20	1.5	160 ± 5	424 ± 5	256 ± 1	405 ± 5	0.05 0.03
21	0.3	0.4	40	25	1.6	185 ± 5	474 ± 1	195 ± 2	464 ± 2	1.45 ± 0.01
22	0.3	0.3	40	20	2	154 ± 10	506 ± 5	339 ± 1	430 ± 1	0.5 ± 0.01

Run order	H_i	d_n	IV	TS	IV/TS	Shear rate at P1 (near substrate)	Shear rate at P2 (max perpend.)	Shear rate at P3 (near nozzle)	Shear rate at P4 (max parallel)	Shear rate at P5 (at relaxing point
23	0.3	0.3	50	25	2	194 ± 10	630 ± 10	421 ± 2	537 ± 1	0.4 ± 0.05
24	0.2	0.3	40	30	1.33	227 ± 5	712 ± 5	333 ± 2	710 ± 2	0.8 ± 0.02
25	0.25	0.4	30	25	1.2	188 ± 5	426 ± 8	206 ± 1	426 ± 1	0.7 ± 0.05
26	0.25	0.3	40	25	1.6	204 ± 5	568 ± 10	271 ± 5	536 ± 10	0.16 ± 0.0.1
27	0.25	0.2	50	25	2	227 ± 5	872 ± 10	597 ± 2	519 ± 2	0.4 ± 0.01

Annex 2: Full factorial design of experiment —3 variables with 3 levels—27 experiments

Run order	H_i	d_n	IV	TS	IV/TS	Shear rate at P1 (near substrate)	Shear rate at P2 (max perpend.)	Shear rate at P3 (near nozzle)	Shear rate at P4 (max parallel)	Shear rate at P5 (at relaxing point)
1	0.2	0.2	30	25	1.2	280 ± 5	540 ± 15	326 ± 5	450 ± 3	0.4 ± 0.05
2	0.2	0.2	40	25	1.6	302 ± 5	738 ± 10	435 ± 2	614 ± 2	0.5 ± 0.02
3	0.2	0.2	50	25	2	328 ± 5	944 ± 15	548 ± 5	778 ± 7	0.6 ± 0.01
4	0.2	0.3	30	25	1.2	278 ± 5	538 ± 2	235 ± 2	537 ± 1	0.4 ± 0.05
5	0.2	0.3	40	25	1.6	310 ± 5	719 ± 10	323 ± 5	719 ± 3	1.15 ± 0.05
6	0.2	0.3	50	25	2	350 ± 5	907 ± 3	410 ± 1	907 ± 2	1.6 ± 0.1
7	0.2	0.4	30	25	1.2	252 ± 5	533 ± 5	266 ± 5	534 ± 5	1.6 ± 0.1
8	0.2	0.4	40	25	1.6	280 ± 5	711 ± 3	366 ± 2	710 ± 1	2 ± 02
9	0.2	0.4	50	25	2	267 ± 10	887 ± 15	468 ± 5	887 ± 3	1.85 ± 0.1
10	0.25	0.2	30	25	1.2	235 ± 15	506 ± 2	360 ± 1	296 ± 6	0.3 ± 0.01
11	0.25	0.2	40	25	1.6	228 ± 5	692 ± 15	480 ± 5	407 ± 5	0.1 ± 0.01
12	0.25	0.2	50	25	2	227 ± 5	872 ± 10	555 ± 2	519 ± 2	0.4 ± 0.01
13	0.25	0.3	30	25	1.2	243 ± 10	414 ± 10	255 ± 3	398 ± 10	0.2 ± 0.01
14	0.25	0.3	40	25	1.6	204 ± 5	568 ± 10	271 ± 5	536 ± 10	0.16 ± 0.0.1
15	0.25	0.3	50	25	2	212 ± 10	722 ± 15	434 ± 5	684 ± 10	0.45 ± 0.02
16	0.25	0.4	30	25	1.2	188 ± 5	426 ± 8	206 ± 1	430 ± 1	0.7 ± 0.05
17	0.25	0.4	40	25	1.6	198 ± 5	572 ± 5	283 ± 5	573 ± 5	1.8 ± 0.1
18	0.25	0.4	50	25	2	200 ± 10	721 ± 8	363 ± 5	725 ± 10	2.5 ± 0.1
19	0.3	0.2	30	25	1.2	144 ± 30	516 ± 10	346 ± 5	206 ± 3	0.25 ± 0.02
20	0.3	0.2	40	25	1.6	218 ± 10	702 ± 5	516 ± 5	289 ± 6	0.18 ± 0.01
21	0.3	0.2	50	25	2	190 ± 10	886 ± 10	634 ± 5	370 ± 7	0.15 ± 0.02
22	0.3	0.3	30	25	1.2	192 ± 10	370 ± 10	200 ± 2	305 ± 1	0.55 ± 0.05
23	0.3	0.3	40	25	1.6	187 ± 15	497 ± 10	260 ± 5	421 ± 5	0.5 ± 0.02
24	0.3	0.3	50	25	2	200 ± 10	630 ± 10	427 ± 2	537 ± 1	0.4 ± 0.05
25	0.3	0.4	30	25	1.2	180 ± 5	346 ± 5	146 ± 2	341 ± 5	0.8 ± 0.01
26	0.3	0.4	40	25	1.6	185 ± 5	474 ± 1	195 ± 5	536 ± 10	0.16 ± 0.0.1
27	0.3	0.4	50	25	2	190 ± 5	604 ± 5	248 ± 2	588 ± 2	0.4 ± 0.01

Acknowledgements This work was supported by Academy of Finland "HiQuench"-project, Grants 334318 and 336287, and "Super20T"-project, Grant 324887.

Funding Open access funding provided by Tampere University (including Tampere University Hospital). Academy of Finland, 334318, Tiina Salmi, 336287, Tiina Salmi, 324887, Tiina Salmi

Data availability The data are made available in the text and appendix in form of tables.

Declarations

Conflict of interest The authors declare that there is no conflict of interest

References

1. Mwema FM, Akinlabi ET (2020) Basics of Fused Deposition Modelling (FDM). In: SpringerBriefs in Applied Sciences and Technology. pp 1–15
2. Ko YS, Herrmann D, Tolar O et al (2019) Improving the filament weld-strength of fused filament fabrication products through improved interdiffusion. Addit Manuf 29:100815. https://doi.org/10.1016/j.addma.2019.100815
3. Liaw C-Y, Tolbert JW, Chow LW, Guvendiren M (2021) Interlayer bonding strength of 3D printed PEEK specimens. Soft Matter 17:4775–4789. https://doi.org/10.1039/D1SM00417D
4. Sanchez LC, Beatrice CAG, Lotti C et al (2019) Rheological approach for an additive manufacturing printer based on material extrusion. Int J Adv Manuf Technol 105:2403–2414. https://doi.org/10.1007/s00170-019-04376-9
5. Zhong Q, Chen Y, Zhang X et al (2024) Correlation between 3D printability and rheological properties of biopolymer fluid: a case study of alginate-based hydrogels. J Food Eng 370:111970. https://doi.org/10.1016/j.jfoodeng.2024.111970
6. Bakrani Balani S, Mokhtarian H, Coatanéa E et al (2023) Integrated modeling of heat transfer, shear rate, and viscosity for simulation-based characterization of polymer coalescence during material extrusion. J Manuf Process 15:108–114. https://doi.org/10.1016/j.jmapro.2023.02.021
7. Bakrani Balani S, Chabert F, Nassiet V, et al (2017) Toward improvement of the properties of parts manufactured by FFF (Fused Filament Fabrication) through understanding the influence of temperature and rheological behaviour on the coalescence phenomenon. In: AIP Conference Proceedings 1896. American Institute of Physics
8. Piau JM, Agassant JF (1996) Rheology for polymer melt processing. Elsevier
9. Fu Y, Downey A, Yuan L et al (2021) In situ monitoring for fused filament fabrication process: a review. Addit Manuf 38:101749. https://doi.org/10.1016/j.addma.2020.101749
10. Colón Quintana JL, Hiemer S, Granda Duarte N, Osswald T (2021) Implementation of shear thinning behavior in the fused filament fabrication melting model: analytical solution and experimental validation. Addit Manuf 37:101687. https://doi.org/10.1016/j.addma.2020.101687
11. Chen J, Smith DE (2021) Filament rheological characterization for fused filament fabrication additive manufacturing: a low-cost approach. Addit Manuf 47:102208. https://doi.org/10.1016/j.addma.2021.102208
12. Al Rashid A, Koç M (2021) Fused filament fabrication process: a review of numerical simulation techniques. Polymers. https://doi.org/10.3390/polym13203534
13. Kattinger J, Ebinger T, Kurz R, Bonten C (2022) Numerical simulation of the complex flow during material extrusion in fused filament fabrication. Addit Manuf 49:102476. https://doi.org/10.1016/j.addma.2021.102476
14. Bakrani Balani S, Chabert F, Nassiet V, Cantarel A (2019) Influence of printing parameters on the stability of deposited beads in fused filament fabrication of poly(lactic) acid. Addit Manuf 25:112–121. https://doi.org/10.1016/j.addma.2018.10.012
15. Bakrani Balani S, Cantarel A, Chabert F, Nassiet V (2018) Influence of parameters controlling the extrusion step in Fused Filament Fabrication (FFF) process applied to polymers using numerical simulation. In: AIP Conference Proceedings 1960
16. Xia H, Lu J, Tryggvason G (2019) A numerical study of the effect of viscoelastic stresses in fused filament fabrication. Comput Methods Appl Mech Eng 346:242–259. https://doi.org/10.1016/j.cma.2018.11.031
17. Sussman M (1994) A level set approach for computing solutions to incompressible two-phase flow. J Comput Phys 114:146–159. https://doi.org/10.1006/jcph.1994.1155
18. Benson DJ (2002) Volume of fluid interface reconstruction methods for multi-material problems. Appl Mech Rev 55:151–165. https://doi.org/10.1115/1.1448524
19. Jacqmin D (1999) Calculation of two-phase Navier–stokes flows using phase-field modeling. J Comput Phys 127:96–127
20. Sussman M, Puckett EG (2000) A coupled level set and volume-of-fluid method for computing 3D and axisymmetric incompressible two-phase flows. J Comput Phys 162:301–337. https://doi.org/10.1006/jcph.2000.6537
21. Bellotti T, Theillard M (2019) A coupled level-set and reference map method for interface representation with applications to two-phase flows simulation. J Comput Phys 392:266–290. https://doi.org/10.1016/j.jcp.2019.05.003
22. Jemison M, Loch E, Sussman M et al (2013) A coupled level set-moment of fluid method for incompressible two-phase flows. J Sci Comput 54:454–491. https://doi.org/10.1007/s10915-012-9614-7
23. Son G, Hur N (2002) A coupled level set and volume-of-fluid method for the buoyancy-driven motion of fluid particles. Numer Heat Transf Part B: Fundam 42:523–542. https://doi.org/10.1080/10407790260444804
24. Mishra AA, Momin A, Strano M, Rane K (2022) Implementation of viscosity and density models for improved numerical analysis of melt flow dynamics in the nozzle during extrusion-based additive manufacturing. Progress Addit Manuf 7:41–54. https://doi.org/10.1007/s40964-021-00208-z
25. Osswald TA, Puentes J, Kattinger J (2018) Fused filament fabrication melting model. Addit Manuf 22:51–59. https://doi.org/10.1016/j.addma.2018.04.030
26. Gilmer EL, Miller D, Chatham CA et al (2018) Model analysis of feedstock behavior in fused filament fabrication: enabling rapid materials screening. Polymer 152:51–61. https://doi.org/10.1016/j.polymer.2017.11.068

27. Mcilroy C, Olmsted P (2016) Deformation of an amorphous polymer during the fused-filament-fabrication method for additive manufacturing. J Rheol doi 10(1122/1):4976839
28. Mackay ME (2018) The importance of rheological behavior in the additive manufacturing technique material extrusion. J Rheol 62:1549–1561. https://doi.org/10.1122/1.5037687
29. Bakrani Balani S, Mokhtarian H, Salmi T, Coatanéa E (2023) An investigation of the influence of viscosity and printing parameters on the extrudate geometry in the material extrusion process. Polymers. https://doi.org/10.3390/polym15092202
30. Mokhtarian H (2019) Product-Process Integrated Meta-Modeling Using a Graph-Based Approach. Tampere University
31. Mokhtarian H, Coatanéa E, Paris H et al (2018) A conceptual design and modeling framework for integrated additive manufacturing. J Mech Des 140:081101. https://doi.org/10.1115/1.4040163
32. Kurtz SM (2012) PEEK biomaterials handbook. Elsevier, pp 75–79
33. Papathanasiou I, Kamposiora P, Papavasiliou G, Ferrari M (2020) The use of PEEK in digital prosthodontics: a narrative review. BMC Oral Health 20:217. https://doi.org/10.1186/s12903-020-01202-7
34. Panayotov IV, Orti V, Cuisinier F, Yachouh J (2016) Polyetheretherketone (PEEK) for medical applications. J Mater Sci: Mater Med 27:118. https://doi.org/10.1007/s10856-016-5731-4
35. Shekar RI, Kotresh TM, Rao PD (2009) Properties of high modulus peek yarns for aerospace applications. J Appl Polym Sci 112:2658–2667. https://doi.org/10.1002/app.29765
36. Dua R, Rashad Z, Spears J et al (2021) Applications of 3d-printed peek via fused filament fabrication: a systematic review. Polymers 13:1–15. https://doi.org/10.3390/polym13224046
37. Cox WP, Merz EH (1958) Correlation of dynamic and steady flow viscosities. J Polymer Sci 28:619–622
38. Schramm G (1994) A practical approach to rheology and rheometry. Gebrueder Haake, Karlsruhe
39. Day M, Sally D, Wiles DM, Chemistry D (1990) Thermal degradation of poly (aryl-Ether- Ether-Ketone): experimental evaluation of crosslinking reactions. J Appl Polym Sci 40:1615–1625. https://doi.org/10.1002/app.1990.070400917
40. Bernd J, Ruthardt A (2014) New die design for a rapid rheological characterization of polymers
41. Acheson DJ (1900) Elementary fluid dynamics. Oxford University Press, Oxford
42. COMSOL Multiphysics (2018) CFD Module User's Guide
43. Bakrani Balani S (2019) Additive manufacturing of the high-performance thermoplastics: Experimental study and numerical simulation of the Fused Filament Fabrication. University of Toulouse
44. Victrex (2014) Victrex ® PEEK 450g
45. Comminal R, Serdeczny MP, Pedersen DB, Spangenberg J (2018) Numerical modeling of the strand deposition flow in extrusion-based additive manufacturing. Addit Manuf 20:68–76. https://doi.org/10.1016/j.addma.2017.12.013
46. Nagarajan HPN, Dimassi S, Haapala KR et al (2019) Knowledge-based design of artificial neural network topology for additive manufacturing process modeling: a new approach and case study for fused deposition modeling. J Mech Des 141:021705. https://doi.org/10.1115/1.4042084